Robust Optimal Framework for Doubly Fed Induction Generator with Uncertain Dynamics

Yongfeng Lü, *Member*, *IEEE*, Xiaowei Zhao, *Member*, *IEEE*, and Priyank Shah

***Abstract*—A robust optimal framework is designed herein to mitigate the oscillatory dynamics in a doubly fed induction generator (DFIG) even in the presence of network disturbances and input variation. To address uncertain dynamics, herein, a novel transformation formula is developed for a wind energy conversion system. An unscented Kalman filter is applied to estimate the unmeasured internal states of the wind energy conversion system using terminal measurements. The detailed convergence and stability analyses of the presented framework are investigated to validate its effectiveness. Additionally, comparative modal analyses are carried out to demonstrate the improvement in the damping of critical low-frequency oscillatory modes using the presented framework. The simulation results demonstrate satisfactory performance under various operating scenarios, such as increasing and decreasing wind speed and varying the terminal voltage. The comparative performance is demonstrated to validate the effectiveness of the presented framework over that of the state-of-the-art frameworks.**

***Index Terms*—Optimal control, power system, renewable energy sources, wind energy conversion system, doubly fed induction generator.**

I. Introduction

Renewable energy sources have exploded into electrical networks to achieve carbon-neutral power generation. Solar photovoltaic and wind energy conversion systems are widely adopted because they have certain advantages [1]. Manifold challenges and recommendations are described in [2] for the grid-integration of the doubly fed induction generator (DFIG)-based wind energy conversion systems [3], [4]. Researchers have highlighted several important problems [5]–[8], such as transient stability issues, protection issues, frequency stability issues, ride-through issues, and resiliency. The importance of system stability and its influencing factors are explicitly discussed in [5]. For instance, reference [6] analyzed the Kalman filter-based control strategy to improve the steady-state and transient stability of a power system. Reference [7] described the use of an adaptive inertia controller to enhance frequency stability even under manifold dynamic scenarios. Due to the flexibilities of converter controllers (e.g., rotor side converters and grid side converters), DFIG-based systems exhibit better dynamic behavior than other types of wind energy conversion systems. Reference [9] analyzed the presence of low-frequency oscillation modes in DFIG-based wind energy conversion systems. Owing to these issues, various state-of-the-art controllers for improving the damping of these modes are described in [10]. Nonetheless, these state-of-the-art methodologies are designed based on the fact that the system model is linearized at one operating point. Subsequently, the system performance may be hampered the presence of disturbances in the network. Moreover, the abovementioned work did not consider DFIG buffeting caused by unknown network disturbances.

To address the above issues, several researchers have analyzed various damping controllers [11] to mitigate oscillations in DFIG-based wind energy conversion systems in the presence of network disturbances. Reference [11] analyzed a coordinated damping controller to improve the system profile via a metaheuristic method. The design procedure is extensively dependent upon the intermediate control parameters, which are obtained with the help of the particle swarm optimization method. This method has several drawbacks [11], such as a low convergence rate and a suboptimal solution. Alleviating some of the shortcomings of [11], [12], hierarchical coordinated control was used to provide effective damping even under a wide range of operating conditions. A power system stabilizer (PSS) is incorporated to provide a positive contribution to dampening these low-frequency oscillations. Nevertheless, the performance of the wind energy generation system is compromised under dynamic operating scenarios because only one of the most dominant system states participates in the feedback controller. Additionally, these

Received: October 20, 2023
Accepted: June 1, 2024
Published Online: September 1, 2024
Yongfeng Lü is with the College of Electrical and Power Engineering, Taiyuan University of Technology, Taiyuan 030024, China (e-mail: lvyilian1989@foxmail.com).
Xiaowei Zhao (corresponding author) and Priyank Shah are with the Intelligent Control and Smart Energy (ICSE) Research Group, School of Engineering, The University of Warwick, Coventry CV4 7AL, UK (e-mail: Xiaowei.Zhao@warwick. ac.uk; p4priyank2909@gmail.com).
DOI: 10.23919/PCMP.2023.000085

state-of-the-art controllers provide a sluggish response because they use a linearized system model to solve the algebraic Riccati equation. To solve some of these issues [12], the sequential quadratic programming approach was applied in [13] to design an optimal damping controller for a large-scale wind energy conversion system. Similarly, a linear-quadratic Gaussian-based controller was designed in [13] to provide a supplementary control signal to the DFIG local controller to inject the modulated active and reactive powers. Nonetheless, the system stability is affected, which may lead to system destabilization under weak grid scenarios. To analyze these issues, reference [14] performed modal analysis to examine the impact of their damping controller and studied the system performance with variations in the grid impedance, stabilization gains, etc. This requires system states and state derivatives, which are difficult to acquire in a real-time power system. To address this issue, the Kalman filter-based solution was designed in [15], [16] to estimate the internal system parameters. Nonetheless, the performance of the system is hampered by uncertain dynamics in the system. Therefore, continuous development of control strategies is required for wind energy conversion systems. Moreover, optimal DFIG control is necessary to guarantee the energy savings and operational performance of wind turbines.

Herein, a robust optimal framework is designed to address the uncertain dynamics of DFIG-based wind energy conversion systems. In contrast with the state-of-the-art frameworks [17], [18], the proposed framework exploits the advantage of a computationally efficient iterative approach [19], [20] to overcome the computational burden of solving Jacobian matrices. The unscented Kalman filter [16] is incorporated with the presented framework to acquire the unmeasurable system states. It has several advantages, such as ease of implementation (i.e., it does not include derivative terms), robustness, and good convergence rate. The presented framework provides satisfactory performance because it has considered full-state feedback, unlike the state-of-art frameworks [17], [18], [21]. Detailed modal analyses are performed herein to validate the stability of the overall system even under wide variations in grid impedance and shaft stiffness. The main advantages of the presented work are described as follows.

1) A robust optimal framework is proposed herein for wind energy conversion systems such that the DFIG can be stable when experiencing uncertain dynamics, i.e., system linearization errors, transmission friction torque and data measurement errors. Detailed mathematical analyses (e.g., learning gain, convergence analysis, and stability analysis) are performed and validated for DFIG-based wind energy conversion systems.

2) A novel transformation formula is developed for the considered system to address uncertain dynamics. The modified algebraic Riccati equation (ARE) is constructed with the help of this designed transformation formula. A novel adaptive law is proposed to learn the solution to the ARE with the predefined performance index.

3) Modal analyses are performed to validate the improvement in the damping of low-frequency modes (e.g., mechanical mode and electromechanical mode) using the presented framework. A detailed eigenvalue chart is plotted to demonstrate the low-frequency oscillating modes with wide variations in grid strength and shaft stiffness.

4) Various comparative performances are demonstrated to validate the effectiveness of the presented framework over the state-of-the-art frameworks [17], [18]. The proposed framework effectively identifies the stabilizing gain in the presence of uncertain dynamics, unlike the state-of-the-art framework [17], [18]. Moreover, the presented framework offers stable operation even under a wide variation in grid impedance; however, state-of-the-art controllers [17], [18] may destabilize the system.

The problem formulation for the DFIG-based wind energy conversion system is described in Section II. The detailed implementation of an adaptive dynamic programming-based robust optimal framework is analyzed in Section III. The stability analysis and modal analysis of the presented work are explicitly examined in Section IV and V. In Section VI, the results and discussion for the presented system are analyzed for various dynamic operating scenarios. The conclusions are described in Section VII.

II. System Modeling and Problem Formulation

In this section, the detailed modeling of the DFIG system [22], [23] and problem formulation are explicitly discussed to derive the robust optimal framework. Figure 1 shows the detailed schematics of the grid-connected DFIG system. In the DFIG system, the stator is directly connected to the grid, and the rotor winding is connected via slip rings to a back-to-back connection of the voltage source converter (VSC). The overall discussion is divided into two sections: 1) modeling of a grid-tied DFIG and 2) problem formulation in compact form.

A. Modeling of a Grid-tied Doubly Fed Induction Generator

The proposed DFIG system can be divided into three subsections: 1) generator modeling; 2) drive train modeling; and 3) back-to-back converter modeling. The detailed explanation of each subsection is provided as follows.

1) Generator Modeling

The voltage equation for the stator and rotor circuit of a dual-fed induction generator is presented as reference frames that rotate at synchronous speeds. The modeling of the DFIG system is expressed as [19]

$$a_1\dot{i}_{qs} = -r_1 i_{qs} + l'_s i_{ds} + \omega_r e'_q - e'_d/\tau_r - v_{qs} + a_m v_{qr} \quad (1)$$

$$a_1\dot{i}_{ds} = -r_1 i_{ds} + l'_s i_{qs} + \omega_r e'_d - e'_q/\tau_r - v_{ds} + a_m v_{dr} \quad (2)$$

$$\dot{e}'_q = \omega_B(r_2 i_{ds} - e'_q/\tau_r + (1-\omega_r)e'_d - a_m v_{dr}) \quad (3)$$

$$\dot{e}'_d = \omega_B(-r_2 i_{qs} - e'_d/\tau_r - (1-\omega_r)e'_q + a_m v_{dr}) \quad (4)$$

where $a_1 = l'_s/\omega_B$, $\tau_r = l_r/r_r$, $e'_d = -\omega_s l_m(i_{qr} + a_m i_{qs})$, $e'_q = -\omega_s l_m(i_{dr} + a_m i_{ds})$, $l'_s = l_s - l_m^2/l_r$, $r_1 = r_2 + r_s$, $r_2 = a_m^2 r_r$, and $a_m = l_m/l_r$. e'_d and e'_q represent the internal equivalent voltages in the *d-q* axis; v_{qr}, v_{dr}, v_{ds} and v_{qs} are the rotor and stator voltage components (p.u.) in the *d-q* axis, respectively; i_{ds} and i_{qs} represent the direct and quadrature axis stator currents in the *d-q* axis, respectively; r_s and r_r represent the resistances of the stators and rotors, respectively; and l_s, l_r and l_m represent the inductances of the stators, rotors, and mutuals, respectively; ω_B is the electrical base speed.

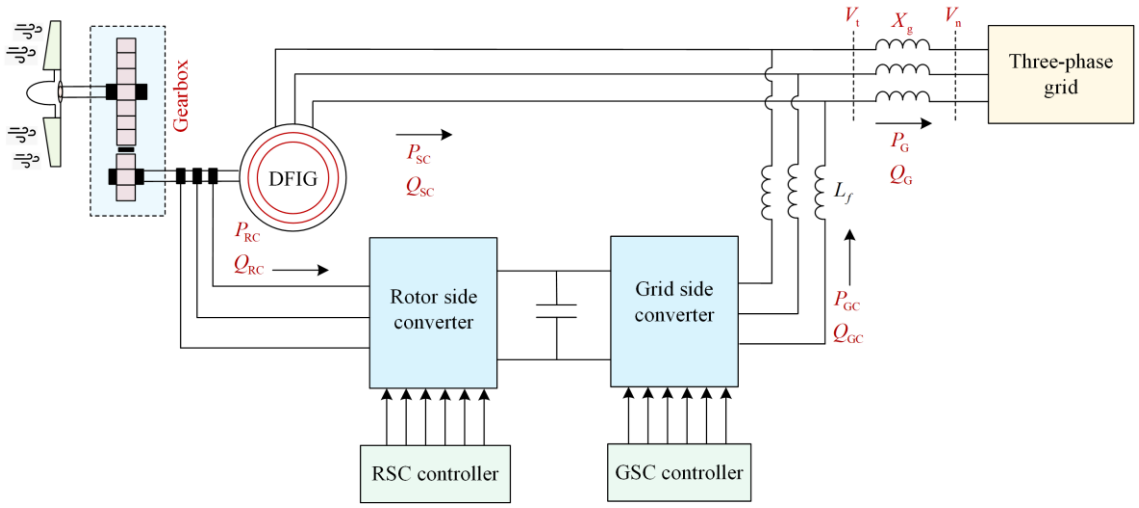

Fig. 1. Schematics of the grid-connected DFIG-based wind energy conversion system.

2) Drive Train Modeling

The two-mass model is adopted herein to represent the wind turbine, unlike the single-mass model. The dynamic characteristics of the drive train are modeled as [24]:

$$2H_g\dot{\omega}_r = T_s - T_e \quad (5)$$

$$2H_g\dot{\omega}_r = T_s - T_e \quad (6)$$

$$\dot{\theta}_{tw} = (\omega_t - \omega_r)\omega_B \quad (7)$$

where H_t and H_g represent the turbine inertia and generator inertia, respectively; ω_t, ω_r, ω_s, and ω_B represent the turbine speed, rotor speed, synchronous speed, and base electrical speed, respectively; P_m, T_s, and T_e represent the input turbine power, shafting generator torques, and electric torques, respectively; and θ_{tw} represents the twist angle. The input turbine power, shaft generator torque, and electrical torque are expressed as

$$P_m = k_{opt} c_p^{pu} v_{wpu}^3 \quad (8)$$

$$T_e = \frac{(e'_q i_{qs} + e'_d i_{ds})}{\omega_s} \quad (9)$$

$$T_s = k_s\theta_{tw} + c_d\dot{\theta}_{tw} \quad (10)$$

where k_{opt} and k_s represent the intermediate optimal constant and shaft stiffness, respectively; c_d and c_p^{pu} represent the damping coefficient and turbine power speed coefficient in p.u., respectively; and v_{wpu} is the wind speed in p.u.

3) Back-to-back Converter Modeling

The back-to-back connected converters are connected with a common direct current (DC) bus capacitor. Both converters play a vital role in regulating the DC bus voltage, supplying active power at the system frequency, and injecting the power at the slip frequency. The total active power (P_e) and reactive power (Q_e) can be obtained as [19]:

$$P_e = v_{ds}i_{qs} + v_{qs}i_{ds} + v_{dr}i_{dr} + v_{qr}i_{qr} \quad (11)$$

$$Q_s = v_{ds}i_{qs} + v_{qs}i_{ds} + v_{dr}i_{qr} + v_{qr}i_{dr} \quad (12)$$

where i_{dr} and i_{qr} represent the direct and quadrature axis rotor currents in the *d-q* axis, respectively.

B. Problem Formulation in Compact Form

An aggregated model represents the wind farm's interconnection with the remainder of the power system, whose electromechanical dynamics are described by algebraic derivatives. The model is represented as

$$\begin{cases} \dot{\boldsymbol{x}}(t) = f(\boldsymbol{x}(t), \boldsymbol{z}(t), \boldsymbol{u}(t)) \\ 0 = g(\boldsymbol{x}(t), \boldsymbol{z}(t), \boldsymbol{u}(t)) \end{cases} \quad (13)$$

where $\boldsymbol{x}(t) \in \mathbb{R}^{n_x}$, $\boldsymbol{u}(t) \in \mathbb{R}^{n_u}$, and $\boldsymbol{z}(t) \in \mathbb{R}^{n_z}$ are the state vectors, control input, and algebraic variables, respectively.

$$\boldsymbol{x}(t) = \begin{bmatrix} i_{qs} & i_{ds} & e'_q & e'_d & \omega_r & \theta_{t\omega} & \omega_t \end{bmatrix}^T \quad (14)$$

$$\boldsymbol{z}(t)=\begin{bmatrix}V_{\mathrm{s}} & \theta_{\mathrm{s}}\end{bmatrix}^{\mathrm{T}} \tag{15}$$

$$\boldsymbol{u}(t)=\begin{bmatrix}v_{dr} & v_{qr}\end{bmatrix}^{\mathrm{T}} \tag{16}$$

where V_{s} and θ_{s} represent the DFIG bus voltage magnitude and phase angle, respectively. To achieve the control target, the controllers v_{dr} and v_{qr} are supplied to the DFIG rotor circuit from the initial state.

C. General Optimal Control

In this section, the nonlinear system model is linearized with Taylor series expansion at an equilibrium point $(\boldsymbol{x}_0, \boldsymbol{y}_0, \boldsymbol{z}_0)$ and can be used to obtain the optimal state feedback control. To execute adaptive dynamic programming [19], [20], the DFIG dynamics are depicted by differential algebraic equations (DAEs) (1). By using the value $(\boldsymbol{x}_0, \boldsymbol{y}_0, \boldsymbol{z}_0)$, (13) is represented as

$$\dot{\boldsymbol{x}}_{\Delta}=\boldsymbol{A}\boldsymbol{x}_{\Delta}+\boldsymbol{B}\boldsymbol{u}_{\Delta} \tag{17}$$

where $\boldsymbol{x}_{\Delta}=(\boldsymbol{x}-\boldsymbol{x}_0)$ and $\boldsymbol{u}_{\Delta}=(\boldsymbol{u}-\boldsymbol{u}_0)$ are the reconstructed system states and input, respectively, and $\boldsymbol{x}_0$ and $\boldsymbol{u}_0$ represent the initial conditions of the DFIG state and input, respectively. Via this method, the problem can be transformed into a regular optimal problem, i.e., obtaining the optimum policy $\boldsymbol{u}_{\Delta}$, driving the DFIG state $\boldsymbol{x}_{\Delta}$ to converge to zero in an optimal manner, such that $\boldsymbol{x}$ can be stabilized to a small compact at approximately $\boldsymbol{x}_0$. Moreover, $\boldsymbol{A}$ and $\boldsymbol{B}$ are defined as

$$\begin{cases}\boldsymbol{A}=\left[\dfrac{\partial f}{\partial \boldsymbol{x}}-\dfrac{\partial f}{\partial \boldsymbol{z}}\left(\dfrac{\partial g}{\partial \boldsymbol{z}}\right)^{-1}\dfrac{\partial g}{\partial \boldsymbol{x}}\right]_{(\boldsymbol{x}_0,\boldsymbol{y}_0,\boldsymbol{z}_0)}\\ \boldsymbol{B}=\left[\dfrac{\partial f}{\partial \boldsymbol{u}}-\dfrac{\partial f}{\partial \boldsymbol{z}}\left(\dfrac{\partial g}{\partial \boldsymbol{z}}\right)^{-1}\dfrac{\partial g}{\partial \boldsymbol{u}}\right]_{(\boldsymbol{x}_0,\boldsymbol{y}_0,\boldsymbol{z}_0)}\end{cases} \tag{18}$$

where $\boldsymbol{A}\in\mathbb{R}^{7\times7}$ and $\boldsymbol{B}\in\mathbb{R}^{7\times2}$ are the turbine DFIG and control voltage matrices, respectively. However, there will be some uncertain dynamics in the modeling process, such as transmission friction torque and data measurement errors. On the other hand, some high orders are omitted in Taylor series expansion modeling. The above mentioned two errors can lead to uncertain dynamics in the system matrix $\boldsymbol{A}$, which can lead to instability of the turbine system with the designed controller.

The system can be stabilized through optimal control (16) with the best performance of the cost function. Linear quadratic regression is a general method for linear systems, where the cost function (J) is given as

$$J=\int_{t}^{\infty}(\boldsymbol{x}_{\Delta}^{\mathrm{T}}\boldsymbol{Q}\boldsymbol{x}_{\Delta}+\boldsymbol{u}_{\Delta}^{\mathrm{T}}\boldsymbol{R}\boldsymbol{u}_{\Delta})\mathrm{d}\tau \tag{19}$$

where $\boldsymbol{Q}\in\mathbb{R}^{n\times n}$ and $\boldsymbol{R}\in\mathbb{R}^{m\times m}$ are the positive definite symmetric matrices. The cost function represents the state performance and the energy cost, which can be adjusted with $\boldsymbol{Q}$ and $\boldsymbol{R}$. The objective of the controller is to obtain an optimal control $\boldsymbol{u}_{\Delta}$, which can drive the DFIG state $\boldsymbol{x}_{\Delta}$ to converge to zero such that $\boldsymbol{x}$ can be stabilized to a small compact at approximately $\boldsymbol{x}_0$. The optimum policy can be defined as

$$\boldsymbol{u}_{\Delta}=-\mathcal{K}_x^{*}\boldsymbol{x}_{\Delta}=-\mathcal{K}_x^{*}(\boldsymbol{x}-\boldsymbol{x}_0) \tag{20}$$

where $\mathcal{K}_x^{*}=\boldsymbol{R}^{-1}\boldsymbol{B}^{\mathrm{T}}\mathcal{P}^{*}$ and $\mathcal{P}^{*}$ is the solution of the following algebraic Riccati equation (ARE)

$$\boldsymbol{A}^{\mathrm{T}}\mathcal{P}+\mathcal{P}\boldsymbol{A}^{\mathrm{T}}+\boldsymbol{Q}-\mathcal{P}\boldsymbol{B}\boldsymbol{R}^{-1}\boldsymbol{B}^{\mathrm{T}}\mathcal{P}=\boldsymbol{0} \tag{21}$$

Figure 2 shows the schematics of the overall structure of the presented framework. Figure 2(a) exhibits the transformation of terminal measurements in the synchronous rotating reference frame. These transformed measurements are further processed to estimate the internal states of DFIG systems, as presented in Fig. 2(b). In this work, the system states are estimated using an advanced filtering technique. The state-of-the-art unscented Kalman filter [16] is adopted herein to observe the internal states of the DFIG system. In contrast with conventional Kalman filters, the unscented Kalman filter has multiple advantages because it does not require a linearization process to acquire the state predictions or covariance matrices and accurately estimates the unknown process and measurement noise. The step-by-step implementation of the unscented Kalman filter is explicitly discussed in the literature [16]. In the presented system, a total of seven state variables ($\boldsymbol{x}_k$) are considered, as mentioned in (14). These estimated system states are fed to the presented robust optimal framework to obtain the optimum gain even in the presence of uncertain dynamics, as depicted in Fig. 2(c).

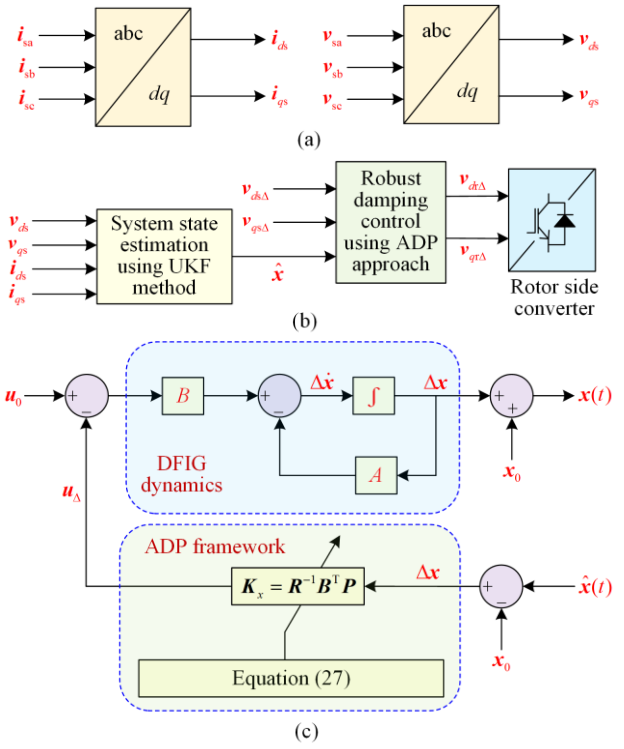

Fig. 2. Overall schematics of the presented controller. (a) Transformation to the *dq*-domain. (b) Consolidated structure of the presented controller. (c) Implementation of the ADP approach.

Remark 1: Although the above optimal policy is effective for the standard linear system, there will be some uncertain nonlinear dynamics that are not considered in the modeling of the turbine system, such as the transmission friction torque and data measurement error. On the other hand, some higher orders are omitted in Taylor series expansion modeling. The abovementioned two errors can lead to uncertain dynamics in the system matrix $\boldsymbol{A}$, which can lead to instability of the turbine system with the designed linear quadratic regulator (LQR) controller.

III. Robust Optimal Framework

In this study, a robust optimal framework is designed to solve the uncertain dynamics that are not considered in the system (17). In this case, the uncertainty range is defined as $d \in D$. Thus, the DFIG model with uncertain dynamics can be given as

$$\dot{\boldsymbol{x}}_\Delta = \boldsymbol{A}(d)\boldsymbol{x}_\Delta + \boldsymbol{B}\boldsymbol{u}_\Delta \tag{22}$$

where $d \in D$ is the unknown DFIG variable dynamic. Model (22) shows that the system dynamics $\boldsymbol{A}$ in (17) contains some uncertainties d, i.e., transmission friction torque, data measurement errors, and some ignored higher orders with Taylor expansion modeling. The algorithm is used to obtain a robust optimal policy to ensure that the DFIG model (22) is asymptotically stable for any $d \in D$.

A. Robust Nominal DFIG Model Formulation

The boundary of the uncertain dynamic is defined first such that the model is reconstructed to design the robust controller. We define $d_0 \in D$ as the nominal value of d. An uncertain dynamic can be transformed in $(\boldsymbol{A}(d)-\boldsymbol{A}(d_0))\boldsymbol{x}_\Delta = \boldsymbol{B}\boldsymbol{\varphi}(d)\boldsymbol{x}_\Delta$ for the bounding vector $\boldsymbol{\varphi}(d) \in \mathbb{R}^{m\times n}$, as presented in [25], [26]. $\mathcal{H} \geqslant 0$ satisfies $\boldsymbol{\varphi}^{\mathrm{T}}(d)\boldsymbol{\varphi}(d) \leqslant \mathcal{H}$, which is known as the matching condition and has been widely researched and applied in engineering, as described in [25]. Here, $\mathcal{H}$ can be used to design the controller to be robust. Therefore, the uncertainty control difficulty of the above DFIG model can be considered when studying the robust policy $\boldsymbol{u}$ to ensure that the nominal DFIG model asymptotically stabilizes for all $d \in D$.

$$\dot{\boldsymbol{x}}_\Delta = \boldsymbol{A}(d_0)\boldsymbol{x}_\Delta + \boldsymbol{B}\boldsymbol{u}_\Delta + \boldsymbol{B}\boldsymbol{\phi}(d)\boldsymbol{x}_\Delta \tag{23}$$

In DFIG modeling, $(\boldsymbol{A}(d_0), \boldsymbol{B})$ can be calculated and is stabilized. Inspired by [26], the robustness difficulty with uncertain dynamics can be regarded as an optimum issue for the DFIG model. Then, the nominal DFIG model of (22) is given as

$$\dot{\boldsymbol{x}}_\Delta = \boldsymbol{A}(d_0)\boldsymbol{x}_\Delta + \boldsymbol{B}\boldsymbol{u}_\Delta \tag{24}$$

The optimal control of the nominal system (24) is obtained to minimize the following value function

$$V(x_\Delta) = \int_t^\infty \left[\boldsymbol{x}_\Delta^{\mathrm{T}}\mathcal{H}\boldsymbol{x}_\Delta + \boldsymbol{x}_\Delta^{\mathrm{T}}\boldsymbol{Q}\boldsymbol{x}_\Delta + \boldsymbol{u}_\Delta^{\mathrm{T}}\boldsymbol{R}\boldsymbol{u}_\Delta\right]\mathrm{d}\tau \tag{25}$$

where $\boldsymbol{Q} \in \mathbb{R}^{n\times n}$ and $\boldsymbol{R} \in \mathbb{R}^{m\times m}$ are the appropriate matrices. $\boldsymbol{x}_\Delta^{\mathrm{T}}\mathcal{H}\boldsymbol{x}_\Delta$ of the value function denotes the robustness of the unknown DFIG dynamics, $\boldsymbol{x}_\Delta^{\mathrm{T}}\boldsymbol{Q}\boldsymbol{x}_\Delta$ represents the state performance, and $\boldsymbol{u}_\Delta^{\mathrm{T}}\boldsymbol{R}\boldsymbol{u}_\Delta$ can minimize the control signals. Thus, by minimizing the cost function, the system state performance and energy can be optimized with the uncertainties in the DFIG model.

Remark 2: The optimum policy of the DFIG model (24) with the value function (25) can asymptotically stabilize the original uncertain DFIG model (22); i.e., the robustness difficulty for the DFIG model (22) with uncertainty is transformed into an optimum issue for the nominal DFIG (24) under the value function (25), as described in [25], [26]. This makes it easier for learning the optimum robust policy of the DFIG with uncertainty dynamics such that the variables can be stabilized with the unknown or uncertain part, e.g., unmodeled system noise and measurement noise.

B. Robust ARE Control

Figure 2(c) shows the overall implementation of the robust ARE controller. One can design a robust state-feedback controller with the help of measurable DFIG model data, which can be regarded as the conventional LQR problem (24). Thus, the optimal control is depicted by

$$\boldsymbol{u}_\Delta^* = -\mathcal{K}_x^*\boldsymbol{x}_\Delta \tag{26}$$

where $\mathcal{K}_x^* = \boldsymbol{R}^{-1}\boldsymbol{B}^{\mathrm{T}}\mathcal{P}^*$. The solution $\mathcal{P}^* \in \mathbb{R}^{n\times n}$ is obtained by

$$\boldsymbol{A}^{\mathrm{T}}(d_0)\mathcal{P}^* + (\mathcal{P}^*)^{\mathrm{T}}\boldsymbol{A}(d_0) + \mathcal{H} + \boldsymbol{Q} - \mathcal{P}^*\boldsymbol{B}\boldsymbol{R}^{-1}\boldsymbol{B}^{\mathrm{T}}\mathcal{P}^* = \boldsymbol{0} \tag{27}$$

The optimal cost function (25) can be obtained from (26) as

$$V^*(\boldsymbol{x}_\Delta(t)) = \int_t^\infty \boldsymbol{x}_\Delta^{\mathrm{T}}(\tau)(\mathcal{H} + \boldsymbol{Q} + \mathcal{K}_x^{\mathrm{T}}\boldsymbol{R}\mathcal{K}_x)\boldsymbol{x}_\Delta(\tau)\mathrm{d}\tau \tag{28}$$

$$V^*(\boldsymbol{x}_\Delta(t)) = \boldsymbol{x}_\Delta^{\mathrm{T}}(\tau)\mathcal{P}^*\boldsymbol{x}_\Delta(\tau) \tag{29}$$

With the differential of (29), we have

$$\begin{aligned}&\dot{\boldsymbol{x}}_\Delta^{\mathrm{T}}(\tau)\mathcal{P}^*\boldsymbol{x}_\Delta(\tau) + \boldsymbol{x}_\Delta^{\mathrm{T}}(\tau)\mathcal{P}^*\dot{\boldsymbol{x}}_\Delta(\tau) + \\ &\boldsymbol{x}_\Delta^{\mathrm{T}}(\tau)(\mathcal{H} + \boldsymbol{Q} + \mathcal{K}_x\boldsymbol{R}\mathcal{K}_x)\boldsymbol{x}_\Delta(\tau) = \boldsymbol{0}\end{aligned} \tag{30}$$

Then, according to (24) and (30), it can be represented as:

$$\begin{aligned}&\boldsymbol{x}_\Delta(\tau)[(\boldsymbol{A}(d_0)\boldsymbol{x}_\Delta - \boldsymbol{B}\mathcal{K}_x)\mathcal{P}^* + \mathcal{P}^*(\boldsymbol{A}(d_0)\boldsymbol{x}_\Delta - \boldsymbol{B}\mathcal{K}_x) + \\ &\mathcal{H} + \boldsymbol{Q} + \mathcal{K}_x\boldsymbol{R}\mathcal{K}_x]\boldsymbol{x}_\Delta(\tau) = \boldsymbol{0}\end{aligned} \tag{31}$$

It is denoted that $\boldsymbol{A}_c = \boldsymbol{A}(d_0)\boldsymbol{x}_\Delta - \boldsymbol{B}\mathcal{K}_x$. Then, the following modified ARE is presented.

$$\boldsymbol{A}_c\mathcal{P}^* + \mathcal{P}^*\boldsymbol{A}_c + \mathcal{H} + \boldsymbol{Q} + \mathcal{K}_x\boldsymbol{R}\mathcal{K}_x = \boldsymbol{0} \tag{32}$$

Then, we can obtain the following Lemma inspired by [27].

Lemma 1: For the nominal DFIG model (24), if the learning gain $\mathcal{K}_x$ is obtained with (27), then the obtained policy is globally optimal.

Proof: From the value function (29), it can be obtained that

$$V^*(\boldsymbol{x}_\Delta)=\dot{\boldsymbol{x}}_\Delta^{\mathrm{T}}(\tau)\mathcal{P}^*\boldsymbol{x}_\Delta(\tau)+\boldsymbol{x}_\Delta^{\mathrm{T}}(\tau)\mathcal{P}^*\dot{\boldsymbol{x}}_\Delta(\tau) \tag{33}$$

$$V^*(x_\Delta)=\boldsymbol{x}_\Delta^{\mathrm{T}}\left[(\boldsymbol{A}(d_0)-\boldsymbol{B}\mathcal{K}_x)\mathcal{P}^*+\mathcal{P}^*(\boldsymbol{A}(d_0)-\boldsymbol{B}\mathcal{K}_x)\right]\boldsymbol{x}_\Delta \tag{34}$$

It can be obtained from (29) and $\boldsymbol{u}_\Delta=-\mathcal{K}_x\boldsymbol{x}_\Delta$ that

$$V^*(\boldsymbol{x}_\Delta(t))=\int_t^\infty \boldsymbol{x}_\Delta^{\mathrm{T}}(\tau)(\mathcal{H}+\boldsymbol{Q}+\mathcal{K}_x^{\mathrm{T}}\boldsymbol{R}\mathcal{K}_x)\boldsymbol{x}_\Delta(\tau)\mathrm{d}\tau+\int_t^\infty\frac{\mathrm{d}}{\mathrm{d}t}(V^*(\boldsymbol{x}_\Delta))\mathrm{d}\tau+V(\boldsymbol{x}_\Delta) \tag{35}$$

$$V^*(\boldsymbol{x}_\Delta(t))=\int_t^\infty \boldsymbol{x}_\Delta^{\mathrm{T}}(\tau)(\mathcal{H}+\boldsymbol{Q}+\mathcal{K}_x^{\mathrm{T}}\boldsymbol{R}\mathcal{K}_x)\boldsymbol{x}_\Delta(\tau)\mathrm{d}\tau+\int_t^\infty \boldsymbol{x}_\Delta^{\mathrm{T}}((\boldsymbol{A}(d_0)-\boldsymbol{B}\mathcal{K}_x)\mathcal{P}^*+\mathcal{P}^*(\boldsymbol{A}(d_0)-\boldsymbol{B}\mathcal{K}_x))\boldsymbol{x}_\Delta\mathrm{d}\tau+V(\boldsymbol{x}_\Delta) \tag{36}$$

$$V^*(\boldsymbol{x}_\Delta(t))=\int_t^\infty \boldsymbol{x}_\Delta^{\mathrm{T}}(\tau)\boldsymbol{G}(\mathcal{K},\mathcal{P}^*)\boldsymbol{x}_\Delta(\tau)\mathrm{d}\tau+V(\boldsymbol{x}_\Delta) \tag{37}$$

where

$$\boldsymbol{G}(\mathcal{K},\mathcal{P}^*)=\mathcal{H}+\boldsymbol{Q}+\mathcal{K}_x^{T}\boldsymbol{R}\mathcal{K}_x+(\boldsymbol{A}(\boldsymbol{d}_0)-\boldsymbol{B}\mathcal{K}_x)\mathcal{P}^*+\mathcal{P}^*(\boldsymbol{A}(\boldsymbol{d}_0)-\boldsymbol{B}\mathcal{K}_x)$$

Then, it can be calculated that

$$\boldsymbol{G}(\mathcal{K}_x,\mathcal{P}^*)=\mathcal{H}+\boldsymbol{Q}+\boldsymbol{A}(d_0)\mathcal{P}^*+\mathcal{P}^*\boldsymbol{A}(d_0)-\mathcal{P}^*\boldsymbol{B}\boldsymbol{R}^{-1}\boldsymbol{B}^{\mathrm{T}}\mathcal{P}^*+\mathcal{K}_x^{\mathrm{T}}\boldsymbol{R}\mathcal{K}_x-\boldsymbol{B}\mathcal{K}_x\mathcal{P}^* \tag{38}$$

$$\boldsymbol{G}(\mathcal{K}_x,\mathcal{P}^*)=\mathcal{H}+\boldsymbol{Q}+\boldsymbol{A}(d_0)\mathcal{P}^*+\mathcal{P}^*\boldsymbol{A}(d_0)-\mathcal{P}^*\boldsymbol{B}\boldsymbol{R}^{-1}\boldsymbol{B}^{\mathrm{T}}\mathcal{P}^*+\mathcal{K}_x^{\mathrm{T}}\boldsymbol{R}\mathcal{K}_x-\boldsymbol{R}\boldsymbol{R}^{-1}\boldsymbol{B}\boldsymbol{R}^{-1}\boldsymbol{B}^{\mathrm{T}}\boldsymbol{P}^*\boldsymbol{P}^* \tag{39}$$

$$\boldsymbol{G}(\mathcal{K}_x,\mathcal{P}^*)=\mathcal{H}+\boldsymbol{Q}+\boldsymbol{A}(d_0)\mathcal{P}^*+\mathcal{P}^*\boldsymbol{A}(d_0)-\mathcal{P}^*\boldsymbol{B}\boldsymbol{R}^{-1}\boldsymbol{B}^{\mathrm{T}}\mathcal{P}^*+(-\boldsymbol{R}^{-1}\boldsymbol{B}^{\mathrm{T}}\mathcal{P}^*+\mathcal{K}_x)\boldsymbol{R}(-\boldsymbol{R}^{-1}\boldsymbol{B}^{\mathrm{T}}\mathcal{P}^*+\mathcal{K}_x) \tag{40}$$

By substituting the standard ARE (27) into (40), it can be shown that

$$V^*(\boldsymbol{x}_\Delta(t))=\int_t^\infty \boldsymbol{x}_\Delta^{\mathrm{T}}(\tau)(\mathcal{K}_x-\mathcal{K}_x^*)\boldsymbol{R}(\mathcal{K}_x-\mathcal{K}_x^*)\boldsymbol{x}_\Delta(\tau)\mathrm{d}\tau+V(\boldsymbol{x}_\Delta) \tag{41}$$

Finally, by calculating the learning gain such that $\mathcal{K}_x-\mathcal{K}_x^*=\boldsymbol{0}$ holds, $\mathcal{K}_x=\mathcal{K}_x^*=\boldsymbol{R}^{-1}\boldsymbol{B}^{\mathrm{T}}\mathcal{P}^*$. The proof is complete.

C. Updating Law for Learning Gains

A novel adaptive data-based estimation can be used to learn the solution to the modified ARE (27) by using the DFIG state. First, Kronecker's product is used to solve the modified ARE (27). The new estimation algorithm is introduced to update the learning parameter gains of the modified ARE. The learning gains $\mathcal{P}^*$ and $\mathcal{K}_x^*$ are updated simultaneously.

To design the robustness of the uncertain DFIG model, Kronecker's product is used, as in [28]. From (27), it can be obtained that

$$\boldsymbol{A}^{\mathrm{T}}(d_0)\mathcal{P}^*+\mathcal{P}^*\boldsymbol{A}(d_0)=-(\mathcal{H}+\boldsymbol{Q}-\mathcal{P}^*\boldsymbol{B}\boldsymbol{R}^{-1}\boldsymbol{B}^{\mathrm{T}}\mathcal{P}^*) \tag{42}$$

Then, it can be obtained that

$$\boldsymbol{x}_\Delta^{\mathrm{T}}(\boldsymbol{A}^{\mathrm{T}}(d_0)\mathcal{P}^*+\mathcal{P}^*\boldsymbol{A}(d_0))\boldsymbol{x}_\Delta=-\boldsymbol{x}_\Delta^{\mathrm{T}}(\mathcal{H}+\boldsymbol{Q}-\mathcal{P}^*\boldsymbol{B}\boldsymbol{R}^{-1}\boldsymbol{B}^{\mathrm{T}}\mathcal{P}^*)\boldsymbol{x}_\Delta \tag{43}$$

A novel online adaptive learning scheme, as in [29], is used to update the optimal $\mathcal{P}^*$ Online. The vec(•) operating and Kronecker algorithms are used in (43). It can be obtained from (43) that

$$(\boldsymbol{x}_\Delta\otimes\boldsymbol{x}_\Delta)^{\mathrm{T}}\mathrm{vec}(\boldsymbol{Q}+\mathcal{H})=(\mathrm{vec}(\boldsymbol{B}\boldsymbol{R}^{-1}\boldsymbol{B}^{\mathrm{T}})\otimes(\boldsymbol{x}_\Delta\otimes\boldsymbol{x}_\Delta))^{\mathrm{T}}\mathrm{vec}(\mathcal{P}^*\otimes\mathcal{P}^*)-2(\boldsymbol{x}_\Delta\otimes\boldsymbol{A}(d_0)\boldsymbol{x}_\Delta)^{\mathrm{T}}\mathrm{vec}(\mathcal{P}^*) \tag{44}$$

A linearly parameterized form (44) can be represented as

$$\boldsymbol{\omega}=-\boldsymbol{\Psi}^{\mathrm{T}}\boldsymbol{\Xi} \tag{45}$$

where $\boldsymbol{\omega}(\boldsymbol{x}_\Delta)=(\boldsymbol{x}_\Delta\otimes\boldsymbol{x}_\Delta)^{\mathrm{T}}\mathrm{vec}(\boldsymbol{Q}+\mathcal{H})$ denotes the DFIG model variables; $\boldsymbol{\Xi}(\boldsymbol{x}_\Delta,\boldsymbol{A},\boldsymbol{B})=[2(\boldsymbol{x}_\Delta\otimes\boldsymbol{A}(d_0)\boldsymbol{x}_\Delta)^{\mathrm{T}},-(\mathrm{vec}(\boldsymbol{B}\boldsymbol{R}^{-1}\boldsymbol{B}^{\mathrm{T}})\otimes(\boldsymbol{x}_\Delta\otimes\boldsymbol{x}_\Delta))^{\mathrm{T}}]^{\mathrm{T}}\in\mathbb{R}^{(n^2+n^4)\times1}$; and $\Psi(\mathcal{P}^*)=\left[\mathrm{vec}(\mathcal{P}^*),\mathrm{vec}(\mathcal{P}^*\otimes\mathcal{P}^*)\right]^{\mathrm{T}}\in\mathbb{R}^{(n^2+n^4)\times1}$.

However, the dimension of $\mathrm{vec}(\mathcal{P}^*\otimes\mathcal{P}^*)$ in (44) and (45) is high, increasing the computational costs in online learning. To reduce the computational cost, the state-feedback learning parameter $\mathcal{K}_x$ is used to supersede $\mathcal{P}^*$ of (43), which can be obtained as

$$\boldsymbol{x}_\Delta^{\mathrm{T}}(\boldsymbol{A}^{\mathrm{T}}(d_0)\mathcal{P}^*+\mathcal{P}^*\boldsymbol{A}(d_0))\boldsymbol{x}_\Delta=-\boldsymbol{x}_\Delta^{\mathrm{T}}(\mathcal{H}+\boldsymbol{Q}-\mathcal{K}_x\boldsymbol{R}\mathcal{K}_x)\boldsymbol{x}_\Delta \tag{46}$$

Then, Kronecker's product function (44) is transformed to

$$2(\boldsymbol{x}_\Delta\otimes\boldsymbol{A}(d_0)\boldsymbol{x}_\Delta)^{\mathrm{T}}\mathrm{vec}(\mathcal{P}^*)+(\boldsymbol{x}_\Delta\otimes\boldsymbol{x}_\Delta)^{\mathrm{T}}\mathrm{vec}(\boldsymbol{Q}+\mathcal{H})-(\mathrm{vec}(\boldsymbol{R})\otimes(\boldsymbol{x}_\Delta\otimes\boldsymbol{x}_\Delta))^{\mathrm{T}}\mathrm{vec}(\mathcal{K}_x^*\otimes\mathcal{K}_x^*)=\boldsymbol{0} \tag{47}$$

where the related terms are transformed to $\boldsymbol{\Xi}(\boldsymbol{x}_\Delta,\boldsymbol{A})=[2(\boldsymbol{x}_\Delta\otimes\boldsymbol{A}(d_0)\boldsymbol{x}_\Delta)^{\mathrm{T}},-(\mathrm{vec}(\boldsymbol{R})\otimes(\boldsymbol{x}_\Delta\otimes\boldsymbol{x}_\Delta))^{\mathrm{T}}]^{\mathrm{T}}$, $\boldsymbol{\Psi}(\boldsymbol{P}^*)=\left[\mathrm{vec}(\mathcal{P}^*),\mathrm{vec}(\mathcal{K}_x\otimes\mathcal{K}_x)\right]^{\mathrm{T}}$, and $\boldsymbol{\omega}(\boldsymbol{x}_\Delta)=(\boldsymbol{x}_\Delta\otimes\boldsymbol{x}_\Delta)^{\mathrm{T}}\ \mathrm{vec}(\boldsymbol{Q}+\mathcal{H})$. After using $(\mathcal{K}_x^*\otimes\mathcal{K}_x^*)$ to replace $(\mathcal{P}^*\otimes\mathcal{P}^*)$ of $\boldsymbol{\Psi}$, the $\boldsymbol{\Psi}$ dimension decreases. Then, the unknown function (47) shows that the parameter $\boldsymbol{\Psi}$ consists of $\mathcal{P}^*$. A new estimation algorithm, as in [29], [30], is introduced to update the unknown parameter $\boldsymbol{\Psi}$ such that the solution $\mathcal{P}^*$ is obtained with an estimation $\hat{\boldsymbol{\Psi}}$ of $\boldsymbol{\Psi}$. To design the updating law, an auxiliary matrix ($\boldsymbol{\mathcal{G}}\in\mathbb{R}^{l\times l}$) and the vector ($\boldsymbol{\phi}\in\mathbb{R}^l$) are given as

$$\begin{aligned}&\dot{\boldsymbol{\mathcal{G}}}=-\ell\boldsymbol{\mathcal{G}}+\boldsymbol{\Xi}\boldsymbol{\Xi}^{\mathrm{T}},\boldsymbol{\mathcal{G}}(0)=\boldsymbol{0}\\&\dot{\boldsymbol{\phi}}=-\ell\boldsymbol{\phi}+\boldsymbol{\Xi}\boldsymbol{\omega},\ \boldsymbol{\phi}(0)=\boldsymbol{0}\end{aligned} \tag{48}$$

where $\ell > 0$ is the filtered gain and $\boldsymbol{\Xi}$ represents the regressor vector. Another vector $\boldsymbol{\Lambda} \in \mathbb{R}^l$ from $\boldsymbol{\mathcal{G}}$ and $\boldsymbol{\phi}$ is defined as

$$\boldsymbol{\Lambda} = \boldsymbol{\mathcal{G}}\hat{\boldsymbol{\Psi}} + \boldsymbol{\phi} \tag{49}$$

with the approximation $\hat{\boldsymbol{\Psi}}$. Then, the updating law of the parameter $\hat{\boldsymbol{\Psi}}$ is designed as

$$\dot{\hat{\boldsymbol{\Psi}}} = -\boldsymbol{\Gamma}\boldsymbol{\Lambda} \tag{50}$$

where $\boldsymbol{\Gamma} > 0$ is the designed learning gain matrix. Then, the optimal approximated learning gain $\hat{\boldsymbol{\mathcal{P}}}$ can be obtained from (45) and (50). From (26), the approximate robust control for the uncertain DFIG model (22) is obtained by

$$\hat{\boldsymbol{u}} = -\hat{\boldsymbol{\mathcal{K}}}_x x_\Delta = -\boldsymbol{R}^{-1}\boldsymbol{B}^{\mathrm{T}}\hat{\boldsymbol{\mathcal{P}}}x_\Delta \tag{51}$$

where $\hat{\boldsymbol{u}}$, $\hat{\boldsymbol{\mathcal{K}}}_x$ and $\hat{\boldsymbol{\mathcal{P}}}$ are approximations of the ideal values $\boldsymbol{u}^*$, $\boldsymbol{\mathcal{K}}_x^*$, and $\boldsymbol{\mathcal{P}}^*$, respectively. From Lemma 1 and Theorem 1, it can be concluded that $\hat{\boldsymbol{\mathcal{K}}}_x \to \boldsymbol{\mathcal{K}}_x^*$ and $\hat{\boldsymbol{\mathcal{P}}} \to \boldsymbol{\mathcal{P}}^*$. As shown in [25], [29], the persisting excitation (PE) of $\boldsymbol{\Xi}$ in (45) holds the positive-definite property of $\boldsymbol{\mathcal{G}}$ in (52).

IV. Stability Analysis

This section presents the estimated parameter convergence and the stability analysis of the uncertain DFIG model (22) with the designed state-feedback robust controller. Then, the following theorem can be given.

Theorem 1: For (45) with estimation algorithm (50), with the PE condition of $\boldsymbol{\Xi}$ in (45), the estimated error ($\tilde{\boldsymbol{\Psi}} = \boldsymbol{\Psi} - \hat{\boldsymbol{\Psi}}$) is proven to converge to zero.

Proof: With the PE condition of $\boldsymbol{\Xi}$, in line with the Lemma in [31], it is shown that $\boldsymbol{\mathcal{G}}$ is positive definite, and $\lambda_{\min}(\boldsymbol{\mathcal{G}}) > \sigma > 0$ holds. The solution of (48) is derived as

$$\begin{aligned} \boldsymbol{\mathcal{G}} &= \int_0^t \mathrm{e}^{-\ell(t-\tau)}\boldsymbol{\Xi}(\tau)\boldsymbol{\Xi}^{\mathrm{T}}(\tau)\mathrm{d}\tau \\ \boldsymbol{\phi} &= \int_0^t \mathrm{e}^{-\ell(t-\tau)}\boldsymbol{\Xi}(\tau)\boldsymbol{\omega}(\tau)\mathrm{d}\tau \end{aligned} \tag{52}$$

Then, from (49), we can obtain that

$$\boldsymbol{\Lambda} = \boldsymbol{\mathcal{G}}\hat{\boldsymbol{\Psi}} + \boldsymbol{\phi} = -\boldsymbol{\mathcal{G}}\tilde{\boldsymbol{\Psi}} \tag{53}$$

The Lyapunov function (V_1) is selected as $V_1 = 0.5(\tilde{\boldsymbol{\Psi}}\boldsymbol{\Gamma}^{-1}\tilde{\boldsymbol{\Psi}})$. From (50) and (53), $\dot{V}_1$ can be obtained as follows:

$$\dot{V}_1 = \tilde{\boldsymbol{\Psi}}\boldsymbol{\Gamma}^{-1}\tilde{\boldsymbol{\Psi}} = -\tilde{\boldsymbol{\Psi}}\boldsymbol{\mathcal{G}}\tilde{\boldsymbol{\Psi}} \leqslant -\sigma\left\|\tilde{\boldsymbol{\Psi}}\right\|^2 \tag{54}$$

where σ is the minimum eigenvalue of $\boldsymbol{\mathcal{G}}$. Thus, from the Lyapunov theorem, $\tilde{\boldsymbol{\Psi}}$ converges to zero exponentially.

For the stability analysis, according to (51), the uncertain DFIG model (24) can be represented by

$$\dot{\boldsymbol{x}}_\Delta = (\boldsymbol{A}(d_0) - \boldsymbol{B}\boldsymbol{R}^{-1}\boldsymbol{B}^{\mathrm{T}}\hat{\boldsymbol{\mathcal{P}}})\boldsymbol{x}_\Delta \tag{55}$$

Moreover, in the DFIG model (24), $\boldsymbol{A}(d_0)$ and $\boldsymbol{B}$ are bounded, i.e., $\|\boldsymbol{A}(d_0)\| \leqslant b_{\mathrm{A}}$, $\|\boldsymbol{B}\| \leqslant b_{\mathrm{B}}$ with $b_{\mathrm{A}} > 0$, $b_{\mathrm{B}} > 0$. Then, the following theorem is presented herein to validate the stability of the designed robust policy.

Theorem 2: For the unknown DFIG model (22), with the approximation of robust state-feedback control (55), the DFIG state variables $\boldsymbol{x}_\Delta$ converge to zero, and the robust control (51) converges to its optimal control (26) of the nominal DFIG model (24).

Proof: A similar proof can be found in [25]; it is omitted here because of limited space.

V. Comparative Performance Analysis

In this section, detailed modal analyses are performed to validate an improvement in the damping of low-frequency oscillation modes, unlike the state-of-the-art controller [18]. Two distinct cases are considered herein to validate the stability of the wind energy conversion system. The detailed analyses are explained as follows.

A. Case-I Modal Analysis with Variations in the Grid Impedance

The comparative eigenvalue analysis of the stator mode between the presented framework and the state-of-the-art controller [18] is illustrated in Figs. 3(a) and (b). As the grid inductance is varied from 0.05 to 0.3, the eigenvalue loci for the state-of-the-art controller are shifted from the left-hand side to the right-hand side of the plane, which indicates the unstable operation of the wind energy conversion system. Figure 3(b) shows the trajectory of the eigenvalue loci obtained from the presented framework. This shows stable operation because the loci are sustained within the left-hand side plane. The presented framework provides optimal control action offered to the DFIG system using an estimation of unmeasured internal states of wind energy conversion systems.

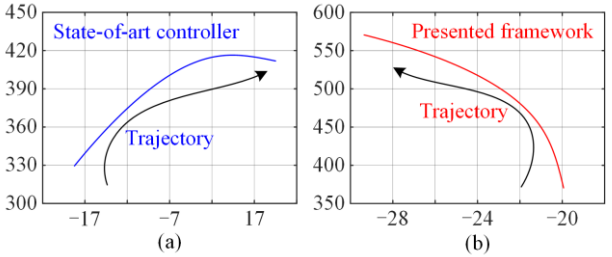

Fig. 3. Detailed modal analysis with varying grid impedance. (a) State-of-the-art methodology. (b) The presented controller.

B. Case-II Modal Analysis with Variations in Shaft Stiffness

Figures 4(a)–(c) show the modal analyses for the state-of-the-art controller [18] with shaft stiffness varying from 0.1 to 0.9. The figure shows the trajectories of the eigenvalues for the stator mode, mechanical mode, and electromechanical mode. Likewise, Figs. 4(d)–(f)

illustrate the trajectory of eigenvalue loci using the presented framework. Figures 4(a)–(f) reveal that the presented framework provides better damping performance than the state-of-the-art controller [18]. The presented framework provides superior performance because it considers full-state feedback, and a stabilized control action is obtained through an iterative adaptive dynamic programming approach-based optimal controller, unlike the state-of-the-art controller [18].

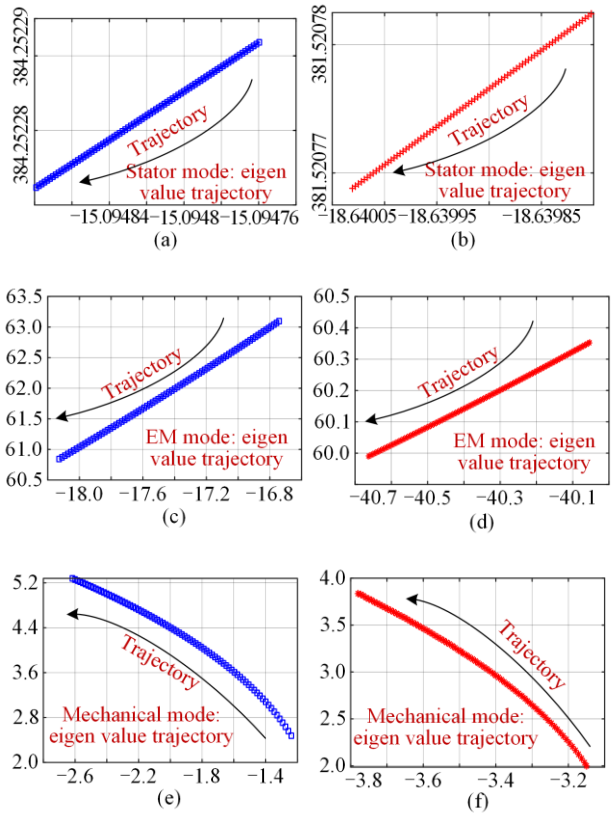

Fig. 4. Detailed modal analysis with variation in shaft stiffness. (a), (c), and (e) State-of-the-art methodology. (b), (d), (f) The presented controller.

Table I presents a comparative quantitative analysis of the modal frequency for the mechanical and electromechanical modes (EMs). This shows that modal damping is significantly strengthened due to the consideration of full-state feedback in the presented framework, unlike in the state-of-the-art controller [18].

TABLE I
COMPARATIVE PERFORMANCE OF MODAL ANALYSIS

Descriptions	State-of-art controller [18]	Presented framework
Modal frequency of the mechanical mode (Hz)	0.55	0.54
Modal frequency of the EM mode (Hz)	9.788	9.581

C. Case-III Comparative Analysis with a State-of-the-art Method

To demonstrate the effectiveness of the presented work, a comparative analysis with the advanced LQR in [32] is carried out in Figs. 5(a) and (b). Figure 5(a) shows the response of several controlled states with the advanced LQR algorithm. One can observe from Fig. 5(a) that the performance in the system states is quite high in several states. However, the presented work effectively exhibits very low overshoots even in the presence of uncertain dynamics (system noise and measurement noise), as depicted in Fig. 5(b). The presented robust controller effectively achieves smooth system dynamics because an advanced adaptive dynamic programming approach is adopted in the presented robust framework to obtain the gain. The salient point of the system performance is observed in Figs. 5(a) and (b).

Moreover, the qualitative analysis between the presented framework and the state-of-the-art controller is analyzed in Table II. This shows that the presented work provides superior performance under manifold cases such as variations in grid impedance and uncertain dynamics. In contrast with the state-of-the-art techniques [12], [18], the presented framework has a low computational burden.

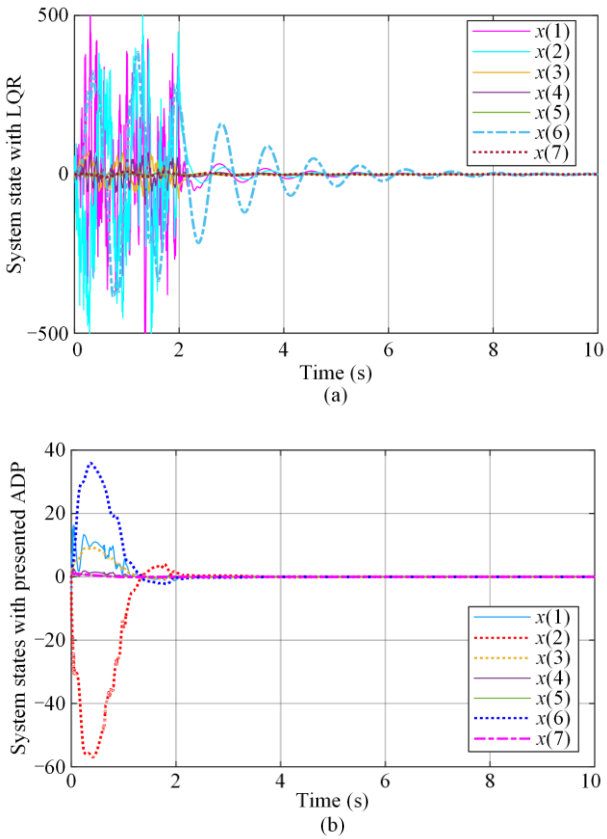

Fig. 5. Comparative performance with the presence of uncertain dynamics. (a) State-of-the-art methodology. (b) Presented work.

TABLE II
COMPARATIVE PERFORMANCE OF THE PRESENTED STRATEGY WITH STATE-OF-THE-ART TECHNIQUES

Description	State-of-art controller [12]	State-of-art controller [18]	Presented work
Type of controller	Power system stabilizer	Linear quadratic regression	Adaptive dynamic programming
Type of feedback	Single-state feedback	Full-state feedback	Full-state feedback
Performance under uncertain dynamics	Not satisfactory	Not satisfactory	Robust and adequate
Performance under variation of grid impedance	Unstable	Unstable	Stable
Computation burden	Low	High	Low
Cost function	0.2981	0.1610	0.1078

Remark 3: Theorem 2 describes the stability analysis, which provides evidence that the proposed controller can stabilize the DFIG system; i.e., the DFIG variables in (22) converge to the command values with the proposed controller (51). Theorem 2 is the theoretical support of Section V, where two examples are provided to verify DIFG stability with the proposed controller. Conversely, Section V is the illustration of Theorem 2.

VI. RESULTS AND DISCUSSION

The DFIG-based wind energy conversion system is modeled in the Matlab environment. An adaptive dynamic programming-based robust damping framework is designed and tested against manifold network disturbances such as a decrease in the wind speed, a sudden increase in the wind speed, and a change in the terminal voltage. The detailed description of each case is as follows.

A. Case-I Response of the System under Variations in Wind Speed from 11 m/s to 7 m/s

Figures 6(a)–(h) illustrate the response of the system variables under sudden variations in the wind speed from 11 m/s to 7 m/s. Figures 6(a)–(d) shows the dynamics of the electrical states of the wind energy conversion system, namely, the direct and quadrature components of current and voltage (I_q, I_d, E_q, and E_d), respectively. As the wind speed decreases from 11 m/s to 7 m/s, the power injection into the grid side network decreases, and the corresponding dynamics are illustrated using significant variation in current components (I_q, I_d). Likewise, the direct and quadrature components of voltages (E_q, E_d) also vary based on variations in the wind speed. The mechanical dynamics of a DFIG are illustrated in Figs. 6(e)–(h). The oscillation in the system quickly dampens due to the full-state feedback of the system states. The presented robust controller provides optimal gains for each participating state compared with the state-of-the-art controller [12], [18]. The variations in the rotor speed and turbine are depicted in Fig. 6(e) and Fig. 6(g), respectively. The minute variation between the rotor speed and turbine speed is observed due to the twist angle, which is depicted in Fig. 6(f). The dynamics of the terminal voltage are depicted in Fig. 6(h).

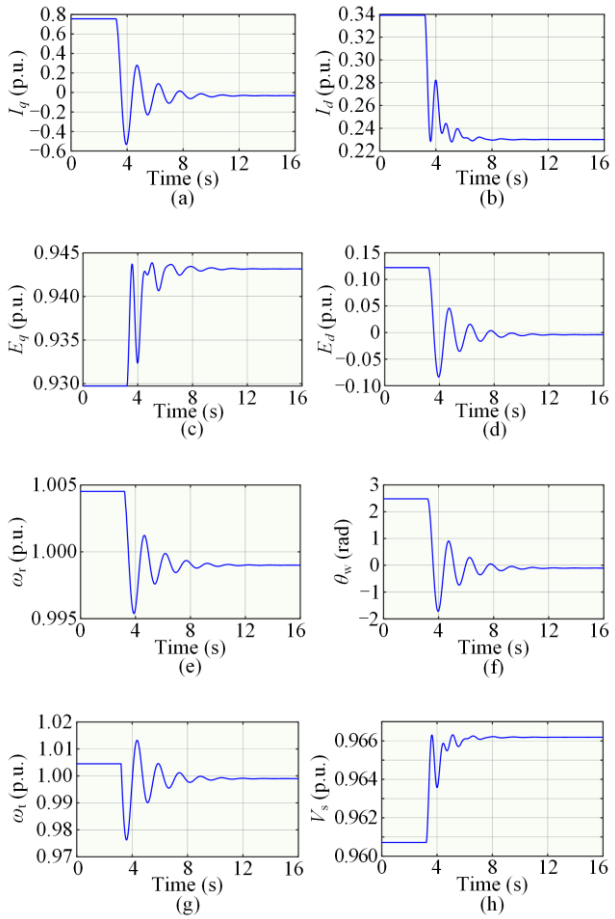

Fig. 6. Response of the DFIG with the proposed controller under various wind speeds from 11 m/s to 7 m/s. (a) Internal current of stator q axe. (b) Internal current of stator d axis. (c) Internal voltage of stator q axis. (d) Internal voltage of stator d axe. (e) Variation of rotor speed. (f) Variation of twist angle. (g) Variation of turbine speed. (h) Terminal voltage.

B. Case-II Response of the System under Variations in Wind Speed from 9 m/s to 11 m/s

Figures 7(a)–(h) demonstrate the behavior of the system under variations in the wind speed from 9 m/s to 11 m/s. The current and voltage dynamics of the system are depicted in Figs. 7(a)–(d). The presented controller effectively provides optimum control gains ($\mathcal{K}_x$) in the

control law to damp out the system oscillations. The oscillation in the current and voltage components is alleviated, thereby mitigating the undesired oscillations in the active power. Figures 7(e)–(h) show the waveforms of the rotor speed, twist angle, turbine speed, and terminal voltage. The rotor and turbine speeds are effectively settled at the new operating point as the wind speed increases from 9 m/s to 11 m/s. The turbine speed increases because of the significant increase in the input kinetic energy of the wind turbine. The corresponding dynamics of the turbine speed and rotor speed are depicted in Fig. 7(g). The dynamics of the terminal voltage are illustrated in Fig. 7(h).

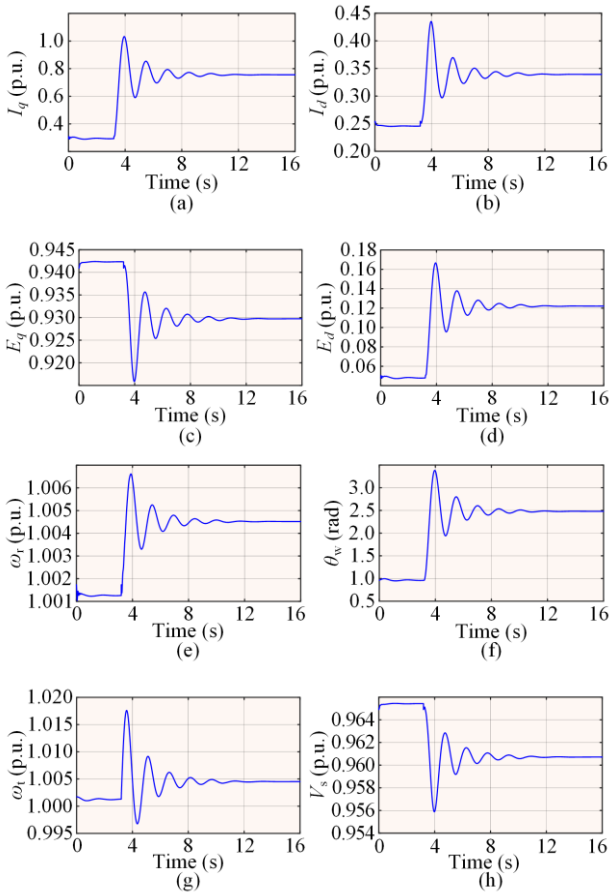

Fig. 7. Response of the DFIG with the proposed controller under various wind speeds from 9 m/s to 11 m/s. (a) Internal current of stator q axe. (b) Internal current of stator d axis. (c) Internal voltage of stator q axis. (d) Internal voltage of stator d axe. (e) Variation of rotor speed. (f) Variation of twist angle. (g) Variation of turbine speed. (h) Terminal voltage.

C. Case III Response of the System under Variations in the Terminal Voltage

Figures 8(a)–(h) show the waveforms of system dynamics under terminal voltage variations from 0.97 p.u. to 0.67 p.u., and the dynamics of I_q, I_d, E_q, E_d, ω_r, θ_w, ω_t, and V_r, respectively. As the terminal voltage decreases to 0.67 p.u., transients in the current and voltage components are observed in Figs. 8(a)–(h). The peak values of the current and voltage components can be suppressed by dissipating the dump load or stored in the energy storage element. The voltage depth is recovered within 200 ms, as clearly illustrated in Fig. 8(h). The oscillations in the current and voltage components are quickly dampened out, as depicted in Figs. 8(a)–(d). The presented controller provides an effective response because it has an inherent capacity to compute the gain matrix ($\mathcal{K}_x$) without any help from predefined system matrices (e.g., the state matrix and input matrix). Likewise, the rotor speed and turbine speed also reached nominal values, as depicted in Fig. 8(e) and Fig. 8(g), respectively. The salient points of this presented controller are illustrated as blue dashed-dotted lines in Figs. 8(a)–(g).

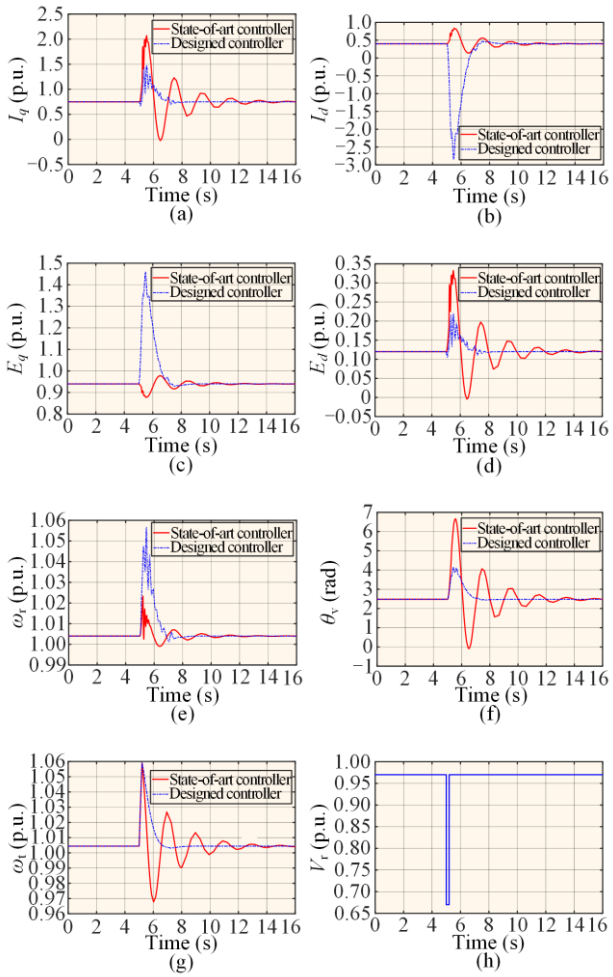

Note: The blue dashed-dotted line represents the proposed robustframework, and the red solid line represents the state-of-the-art controller.

Fig. 8. Comparison of the response to state-of-the-art control in [33] under various terminal voltages from 0.97 p.u. to 0.67 p.u. (a) Internal current of stator q axe. (b) Internal current of stator d axis. (c) Internal voltage of stator q axis. (d) Internal voltage of stator d axe. (e) Variation of rotor speed. (f) Variation of twist angle. (g) Variation of turbine speed. (h) Terminal voltage variation.

To show the advantage of the proposed robust optimal controller, the comparison results with the scaled current tracking control in [33] are added to Figs. 8(a)–(g) as red solid lines. The results in Figs. 8(a)–(g) show that compared with recent DFIG approaches, the proposed method can make the DFIG variables converge faster with less chattering and uncertain variations in the terminal voltage. However, the overshoots with the proposed framework are high in Figs. 8(b) and (c), which is another constraint control problem to be addressed in future work.

Remark 4: To guarantee the stabile property of a DFIG with uncertain grid faults, several novel control frameworks are proposed. A novel parallel cooperative scheme is proposed to enhance a low-voltage ride-through (LVRT) capacity DFIG-based wind farm and inject reactive current during grid faults in [34]. An excitation converter with a parallel scheme is proposed for severe grid faults in [35], where experimental verification is provided to validate the proposed method. A scaled current tracking control is proposed for a rotor-side converter (RSC) to enhance its LVRT capacity under grid faults in [33]. However, these studies did not consider the optimal performance of the DFIG and did not analyze the stability of the proposed fault control. This paper proposes a robust optimal framework to effectively address the above issues under variations in the terminal voltage.

VII. Conclusions

An adaptive dynamic programming-based robust framework is presented for the optimal operation of a DFIG-based wind energy conversion system. The presented framework has the following advantages: 1) it does not require solving nonlinear algebraic Riccati equations, which significantly reduces the computational burden, unlike linear quadratic regulators; 2) to provide robust performance against uncertain dynamics, a novel transformation formula is developed and demonstrates satisfactory performance, unlike a state-of-the-art controller; and 3) detailed mathematical analysis (e.g., learning gain, convergence analysis, and stability analysis) is explicitly performed to validate the robustness characteristics of the presented control law. The modal analyses demonstrate that the presented DFIG-based wind energy conversion system provides stable operation and significantly improves the transient stability margin, unlike state-of-the-art controllers. The simulation results demonstrate a satisfactory response with manifold operating scenarios. The quantitative and qualitative analyses demonstrated the effectiveness of the presented framework for different disturbance scenarios. In future work, the robust optimal controls of DFIGs that consider variable constraints will be studied.

Appendix A

TABLE A1 The Main Parameters and Their Value

Parameters	Value
β	0
$C_{\mathrm{p}}^{\max}$	0.48
X_{e}	0.06
X_{m}	4
k	0.3
c	0.01
H_{t}	4 s
H_{g}	$0.1\,H_{\mathrm{t}}$
l_{m}	4 p.u.
l_{s}	$1.01\,l_{\mathrm{m}}$
l_{r}	$1.005\,l_{\mathrm{s}}$
r_{s}	$l_{\mathrm{m}}/800$
r_{r}	$1.1\,r_{\mathrm{s}}$
T_{r}	738.2181
k	0.3 p.u./el.rad
V_{g}	1

Acknowledgment

Not applicable.

Authors' Contributions

Yongfeng Lü: full-text writing and the construction of the paper framework, part of software and simulations. Xiaowei Zhao: conceptualization, investigation, resources, supervision, review & editing. Priyank Shah: part of software and simulations. All authors read and approved the final manuscript.

Funding

This work is supported in part by the National Natural Science Foundation of China (No. 62103296), the UK Engineering and Physical Sciences Research Council (No. EP/T021713/1), and the Shanxi Scholarship Council of China (No. 2023-062).

Availability of Data and Materials

Not applicable.

Declarations

The authors declare that they have no known competing financial interests or personal relationships that could have appeared to influence the work reported in this article.

Authors' Information

Yongfeng Lü received the B.S. and M.S. degrees in mechatronic engineering from Faculty of Mechanical and Electrical Engineering, Kunming University of Science and Technology, Kunming, China, in 2012 and

2016, and the Ph.D. degree in control science and engineering with the School of Automation, Beijing Institute of Technology, Beijing, China, in 2020. From 2021 to 2022, he worked as a research fellow with the School of Engineering, University of Warwick, Coventry, UK. Currently, he is an associate professor with the College of Electrical and Power Engineering, Taiyuan University of Technology, Taiyuan, China. His current research interests include intelligent control, adaptive dynamic programming, smart energy systems and servo systems.

Xiaowei Zhao obtained the Ph.D. degree in control theory from Imperial College London in 2010. After that he worked as a postdoctoral researcher at the University of Oxford for three years. He joined Warwick in 2013. At present, he is a professor of control engineering and an EPSRC fellow at the School of Engineering, University of Warwick, Coventry, UK. His main research areas are control theory and machine learning with applications on offshore renewable energy systems, local smart energy systems, and autonomous systems.

Priyank Shah received the B.Eng. in electrical engineering from Birla Vishvakarma Mahavidyalaya, Vallabh Vidyanagar, India, in 2013, and the M.Tech. degree in power system and the Ph.D. degree in electrical engineering from the Indian Institute of Technology Delhi, New Delhi, India, in 2015 and 2020, respectively. He is currently working as a research fellow with the Intelligent Control and Smart Energy Research Group, University of Warwick, Coventry, UK. His research interests include synchronization, grid-connected power electronics converter, virtual synchronous generator, fault ride through operation, leakage current, and power quality.

REFERENCES

[1] F. Blaabjerg and K. Ma, "Wind energy systems," *Proceedings of the IEEE*, vol. 105, no. 11, pp. 2116-2131, Nov. 2017.

[2] S. D. Ahmed, F. S. Al-Ismail, and M. Shafiullah *et al.*, "Grid integration challenges of wind energy: a review," *IEEE Access,* vol. 8, pp. 10857-10878, Jan. 2020.

[3] B. Li, D. Zheng, and B. Li *et al.*, "Analysis of low voltage ride-through capability and optimal control strategy of doubly-fed wind farms under symmetrical fault," *Protection and Control of Modern Power Systems,* vol. 8, no. 1, pp. 1-15, Jul. 2023.

[4] S. Mensou, A. Essadki, and T. Nasser *et al.*, "A direct power control of a DFIG based-WECS during symmetrical voltage dips," *Protection and Control of Modern Power Systems,* vol. 5, pp. 1-12, Jan. 2020.

[5] Y. Liu, A. K. Singh, and J. Zhao *et al.*, "Dynamic state estimation for power system control and protection," *IEEE Transactions on Power Systems*, vol. 36, no. 6, pp. 5909-5921, Nov. 2021.

[6] J. Liu, W. Yao, and J. Wen *et al.*, "Impact of power grid strength and PLL parameters on stability of grid-connected DFIG wind farm," *IEEE Transactions on Sustainable Energy*, vol. 11, no. 1, pp. 545-557, Jan. 2020.

[7] H. Lao, L. Zhang, and T. Zhao *et al.*, "Innovated inertia control of DFIG with dynamic rotor speed recovery," *CSEE Journal of Power and Energy Systems*, vol. 8, no. 5, pp. 1417-1427, Sep. 2020.

[8] J. Ren, X. Xiao, and Z. Zheng *et al.*, "Impact of phase angle jump on DFIG under LVRT conditions: challenges and recommendations," *IEEE Transactions on Power Delivery*, vol. 36, no. 6, pp. 3701-3713, Dec. 2021.

[9] J. Morato, T. Knüppel, and J. Østergaard, "Residue-based evaluation of the use of wind power plants with full converter wind turbines for power oscillation damping control," *IEEE Transactions on Sustainable Energy*, vol. 5, no. 1, pp. 82-89, Jan. 2013.

[10] M. A. Hannan, N. N. Islam, and A. Mohamed *et al.*, "Artificial intelligent based damping controller optimization for the multi-machine power system: a review," *IEEE Access*, vol. 6, pp. 39574-39594, Jul. 2018.

[11] W. C. Wong and C. Chung, "Coordinated damping control design for DFIG-based wind generation considering power output variation," *IEEE Transactions on Power Systems*, vol. 27, no. 4, pp. 1916-1925, 2012.

[12] T. Surinkaew and I. Ngamroo, "Hierarchical co-ordinated wide area and local controls of DFIG wind turbine and PSS for robust power oscillation damping," *IEEE Transactions on Sustainable Energy*, vol. 7, no. 3, pp. 943-955, Jul. 2016.

[13] N. Gurung, R. Bhattarai, and S. Kamalasadan, "Optimal oscillation damping controller design for large-scale wind integrated power grid," *IEEE Transactions on Industry Applications*, vol. 56, no. 4, pp. 4225-4235, Jul. 2020.

[14] L. Chen, Y. Min, and Y. Chen *et al.*, "Evaluation of generator damping using oscillation energy dissipation and the connection with modal analysis," *IEEE Transactions on Power Systems*, vol. 29, no. 3, pp. 1393-1402, May 2014.

[15] A. S. Mir and N. Senroy, "DFIG damping controller design using robust CKF-based adaptive dynamic programming," *IEEE Transactions on Sustainable Energy*, vol. 11, no. 2, pp. 839-850, Apr. 2020.

[16] E. A. Wan and R. Van Der Merwe, "The unscented Kalman filter for nonlinear estimation," in *Proceedings of the IEEE 2000 Adaptive Systems for Signal Processing*, *Communications*, *and Control Symposium (Cat. No. 00EX373)*, Lake Louise, AB, Canada, Oct. 2000, pp. 153-158.

[17] M. E. Aboul-Ela, A. Sallam, and J. D. McCalley *et al.*, "Damping controller design for power system oscillations using global signals," *IEEE Transactions on Power Systems*, vol. 11, no. 2, pp. 767-773, May 1996.

[18] F. Lewis, "Optimal feedback control: practical performance and design algorithms for industrial and aerospace systems," *UTA Research Institute The University of Texas at Arlington*, Texas, USA, Jan. 2012.

[19] W. Guo, F. Liu, and J. Si *et al*., "Online supplementary ADP learning controller design and application to power system frequency control with large-scale wind energy integration," *IEEE Transactions on Neural Networks and Learning Systems*, vol. 27, no. 8, pp. 1748-1761, Aug. 2015.

[20] Y. Tang, H. He, and Z. Ni *et al*., "Adaptive modulation for DFIG and STATCOM with high-voltage direct current transmission," *IEEE Transactions on Neural Networks and Learning Systems*, vol. 27, no. 8, pp. 1762-1772, Aug. 2016.

[21] A. Latif, S. S. Hussain, and D. C. Das *et al*., "State-of-the-art of controllers and soft computing techniques for regulated load frequency management of single/multi-area traditional and renewable energy based power systems," *Applied Energy*, vol. 266, May 2020.

[22] S. Li, J. Ye, and D. Chen, "Passive control strategy to mitigate sub-synchronous control interaction of DFIG-based integrated power systems," *Power System Protection and Control*, vol. 51, No. 11, Jun. 2023, pp. 77-85. (in Chinese)

[23] A. S. Tummala, "A robust composite wide area control of a DFIG wind energy system for damping inter-area oscillations," *Protection and Control of Modern Power Systems*, vol. 5, no. 3, pp. 260-269, Jul. 2020.

[24] J. Hu, Y. Huang, and D. Wang *et al*., "Modeling of grid-connected DFIG-based wind turbines for DC-link voltage stability analysis," *IEEE Transactions on Sustainable Energy*, vol. 6, no. 4, pp. 1325-1336, Oct. 2015.

[25] J. Na, J. Zhao, and G. Gao *et al*., "Output-feedback robust control of uncertain systems via online data-driven learning," *IEEE Transactions on Neural Networks and Learning Systems*, vol. 32, no. 6, pp. 2650-2662, Jun. 2020.

[26] F. Lin, "An optimal control approach to robust control design," *International Journal of Control*, vol. 73, no. 3, pp. 177-186, Nov. 2000.

[27] Y. Jiang and Z. Jiang, "*Robust adaptive dynamic programming*," John Wiley & Sons, 2017.

[28] Y. Jiang and Z. Jiang, "Computational adaptive optimal control for continuous-time linear systems with completely unknown dynamics," *Automatica*, vol. 48, no. 10, pp. 2699-2704, Oct. 2012.

[29] Y. Lü, H. Chang, and J. Zhao, "Online adaptive integral reinforcement learning for nonlinear multi input system," *IEEE Transactions on Circuits and Systems II*: *Express Briefs*, vol. 7, no. 11, pp. 4176-4180, May 2023.

[30] Y. Lü, J. Zhao, and R. Li *et al*., "Robust optimal control of the multi-input systems with unknown disturbance based on adaptive integral reinforcement learning Q-function," *International Journal of Robust and Nonlinear Control*, vol. 34, no. 6, pp. 1-10, Apr. 2024.

[31] Y. Lü, J. Na, and X. Zhao *et al*.,"Multi-H∞ controls for unknown input-interference nonlinear system with reinforcement learning," *IEEE Transactions on Neural Networks and Learning Systems*, vol. 34, no. 9, pp. 5601-5613, Sep. 2023.

[32] C. Mu, Q. Zhao, and C. Sun *et al*., "An ADDHP-based Q-learning algorithm for optimal tracking control of linear discrete-time systems with unknown dynamics," *Applied Soft Computing*, vol. 82, Sep. 2019.

[33] Q. Huang, X. Zou, and D. Zhu *et al*., "Scaled current tracking control for doubly fed induction generator to ride-through serious grid faults," *IEEE Transactions on Power Electronics*, vol. 31, no. 3, pp. 2150-2165, Mar. 2015.

[34] X. Xiao, R. Yang, and Z. Zheng *et al*., "Cooperative rotor-side SMES and transient control for improving the LVRT capability of grid-connected DFIG-based wind farm," *IEEE Transactions on Applied Superconductivity*, vol. 29, no. 2, pp. 1-5, Mar. 2019.

[35] J. Gu, "Enhanced excitation converter with parallel/series DC-link based on TAB for DFIG to improve the LVRT capability under severe grid faults," *IEEE Transactions on Power Electronics*, vol. 38, no. 10, pp. 12304-12308, Oct. 2023.